CrystEngComm

Accepted Manuscript

ROYAL SOCIETY OF CHEMISTRY

www.rsc.org/crystengcomm

Cite this: DOI: 10.1039/c0xx00000x

www.rsc.org/xxxxxx

ARTICLE TYPE

Controllable Synthesis and Size-dependent Upconversion Luminescence Properties of Lu_2O_3:Yb^{3+}/Er^{3+} Nanospheres

Kezhi Zheng, Weiye Song, Changjian Lv, Zhenyu Liu, and Weiping Qin*

Received (in XXX, XXX) Xth XXXXXXXXX 201X, Accepted Xth XXXXXXXXX 201X
DOI: 10.1039/b000000x

Lu_2O_3:Yb^{3+}/Er^{3+} nanocrystals with various sizes and shapes (nano-aggregates, sub-micrometer wires, and nanospheres) have been synthesized by the soft chemistry coprecipitation route. By regulating the reactant ratio of rare earth to urea precipitant ([RE^{3+}]/$(NH_2)_2CO$), uniform spherical Lu_2O_3:Yb^{3+}/Er^{3+} nanoparticles with the sizes of 45 nm, 100 nm, 165 nm, 200 nm, and 250 nm were obtained in the experiments. The phases, morphologies, as well as the luminescence properties of as-prepared samples were characterized by means of X-ray diffraction (XRD), scanning electron microscopy (SEM), and upconversion luminescence (UCL) spectra, respectively. Under the excitation of 980 nm diode laser, the Lu_2O_3:Yb^{3+}/Er^{3+} samples showed size-dependent upconversion luminescence property. From the results of Fourier transform infrared (FTIR) spectra and dynamical analysis, it was confirmed that the surface effect is dominant in influencing the UCL of Er^{3+} in the spherical Lu_2O_3:Yb^{3+}/Er^{3+} samples. By coating Lu_2O_3:Yb^{3+}/Er^{3+} nanospheres with different shell layers, UCLs of Er^{3+} were changed greatly in these core-shell samples. The possible physical mechanism involved in size/surface-dependent upconversion processes were discussed in detail.

Introduction

The conversion of infrared (IR) or near-infrared (NIR) photons to higher energy ultraviolet (UV) or visible light *via* multiple absorptions or energy transfers (ET), known as upconversion luminescence (UCL), is an area of extensive research due to its fundamental interest and potential for photonics applications.[1–4] Rare earth ions (RE^{3+}) doped UCL materials, owing to their unique optical properties arising from the intra *4f* transitions of RE^{3+}, attracted many attentions these years owing to their extensively employed in the fields of lasers, three-dimensional displays, biomedicine, next-generation lighting, *etc*.[5–13] Among all the RE^{3+}, Er^{3+} is an ideal candidate for UCL since its rich and ladder-like electronic energy level structure. In addition, Yb^{3+} has a relative large absorption cross section around 980 nm□□ and a long excited state lifetime, and it is often chosen as a codopant in UCL materials. It is well-known that the UCL of Er^{3+} is sensitive to many factors, such as particle size, doping concentration, temperature, pumping power, and so on.[14–19] However, up to now, it has still been a great challenge for researchers to elucidate the influence of particle size on UCL properties clearly, owing to the obstacle in synthesizing particles with a uniform size. Therefore, further works are still necessary for obtaining suitable samples and investigating their luminescence properties in detail, because it is beneficial to understand the complex size-dependent UCL mechanism in the codoped systems.

Generally, UCL materials are typically composed of an inorganic matrix and dopant RE^{3+} ions embedded in its host lattice. Besides the particle size, temperature, pumping power and the nature of the active ions, the efficiency of upconversion luminescence is strongly dependent on the phonon energies of the host materials. Therefore, a selection of appropriate host materials is essential in the synthesis of RE^{3+} doped UCL materials with favorable optical properties. Among the rare earth oxides, cubic Lu_2O_3 has been considered to be one of the most excellent host materials for RE^{3+} doping due to its high mass density (9.4 g cm^{-3}), good phase stability, low thermal expansion, low phonon energy (phonon cutoff ≈ 600 cm^{-1}), and broad optical transparence from the visible to the NIR regions.[20–24] Up to now, cubic Lu_2O_3 with various sizes and shapes (nanofibers, nanorods, and flower-like microstructure, *etc*) have been synthesized by numerous routes such as co-precipitation, sol-gel, hydrothermal/solvothermal, electrospinning, and so on.[25–28] Although it is well accepted that uniform spherical nanoparticles with lower surface defects are preferred to be used as phosphor materials, effort in synthesizing uniform nano luminescent materials, especially in synthesizing uniform Lu_2O_3 nanospheres, is lacking. More importantly, the top of the valence-band energy levels of Lu-based oxides are mainly composed of Lutetium 4f orbital, whereas in Y-based materials, the corresponding top

levels are mostly oxygen 2p orbital. This difference make Lu-based compounds to be more favorable host materials than Y-based compounds for the UCL of RE^{3+} owing to the intensity-borrowing mechanism, as proposed by Guillot-Noel *et al*.[29] In 2002, John A. Capobianco *et al* have reported that the UCL of Er^{3+} in Lu_2O_3 host is stronger than that in Y_2O_3 phosphor.[30] Furthermore, many other investigations about RE^{3+} doped Lu-based compounds, such as Nd^{3+} doped $LuVO_4$, Ce^{3+}/Pr^{3+}/Tm^{3+}-Ho^{3+} doped $LuLiF_4$, and Tm^{3+}/Er^{3+} doped $NaLuF_4$, have been proved to be stronger luminescence and better laser performance than their corresponding Y-based compounds as well.[31–37] Despite the fact that some novel spectral phenomena have been observed in RE^{3+} doped Lu-based compounds, few systematic studies on size-dependent UCL behavior were reported to date.

Herein, we report the controllable synthesis of Yb^{3+}-Er^{3+} codoped Lu_2O_3 nanocrystals *via* a simple soft chemistry co-precipitation method followed by a subsequent calcinations process. Lu_2O_3:Yb^{3+}/Er^{3+} nanocrystals with various sizes and shapes (nano-aggregates, sub-micrometer wires, and uniform nanospheres) were synthesized using different precipitants. Different-sized Lu_2O_3 nanospheres were obtained by regulating the reactant ratio of rare earth to urea precipitant. The influences of particle size and surface coating on the UCL properties of Lu_2O_3:Yb^{3+}/Er^{3+} nanospheres were studied systemically. The size-dependent UC population and dynamical decay are discussed here in detail.

Experimental procedures

Chemicals

All chemicals were of analytical grade and used without further purification. $Lu(NO_3)_3{\cdot}6H_2O$ (99.999%), $Yb(NO_3)_3{\cdot}6H_2O$ (99.999%), and $Er(NO_3)_3{\cdot}6H_2O$ (99.999%) were supplied by Yutai Qingda Chemical Technology Co., Ltd. China. Urea ($(NH_2)_2CO$), Ammonium bicarbonate (NH_4HCO_3), ammonium hydroxide (NH_4OH) and tetraethoxysilane (TEOS) were supplied by Beijing Fine Chemical Company.

Sample Preparation

a) Synthesis of Lu_2O_3 Nanocrystals

Stoichiometric (mol%) of $Lu(NO_3)_3{\cdot}6H_2O$, $Yb(NO_3)_3{\cdot}6H_2O$, and $Er(NO_3)_3{\cdot}6H_2O$ were dissolved into deionized water, resulting in the formation of colorless solutions of $RE(NO_3)_3$ (RE = Lu, Yb, and Er). $(NH_2)_2CO$ and NH_4HCO_3 were dissolved into deionized water to form the corresponding precipitant water solutions as well. Yb^{3+}-Er^{3+} codoped Lu_2O_3 powder samples were prepared by using a procedure described briefly as follows.[38] In a typical synthesis, 0.47 mmol of $Lu(NO_3)_3$, 0.025 mmol of $Yb(NO_3)_3$, and 0.005 mmol of $Er(NO_3)_3$ aqueous solutions were added to 50 mL of deionized water to form a clear solution in a reaction bottle under vigorously stirring. Then aqueous urea solution was added into the stirring solution dropwise and under magnetic stirring. Subsequently, the above solution was heated at 85°C for 5 h in order to decompose the urea. The resulting suspension aged during 24 h and then the precursor was separated by centrifugation, washed several times with deionized water and ethanol and dried at 80°C. Finally, the as-prepared amorphous samples were annealed at 850°C for 2 h in air to obtain the Lu_2O_3:5%Yb^{3+}/1%Er^{3+} products. Different amounts of $(NH_2)_2CO$ were added into the reactant solutions to regulate the particle sizes of as-prepared Lu_2O_3 samples. Additionally, in the cases of synthesis with the NH_4HCO_3 and NH_4OH precipitants, the samples were prepared with the synthetic conditions unchanged as described above, except for introducing proper amount of NH_4HCO_3 and NH_4OH solution instead of $(NH_2)_2CO$.

b) Coating of Lu_2O_3:Yb^{3+}/Er^{3+} nanospheres with SiO_2 Shells

Stöber method was adopted for the SiO_2 coating process.[39] Firstly, 100 mg of the annealed Lu_2O_3:Yb^{3+}/Er^{3+} nanospheres were dispersed in a mixture of distilled water (3 mL) and ethanol (20 mL) by sonication for 15 min. Secondly, 1 mL of ammonia (25 wt%) was added slowly into the solution under stirring. Here, ammonia was used to catalyze the hydrolysis and condensation reactions of TEOS. Under stirring for a few minutes, 1 mL of TEOS was added dropwise to the above solution at room temperature. After continuous stirring for another 24 h, the mixture was centrifuged and washed with ethanol three times. The white-colored powder sample of Lu_2O_3:Yb^{3+}/Er^{3+}@SiO_2 was obtained after dried at 80°C in air for 20 h.

c) Coating of Lu_2O_3:Yb^{3+}/Er^{3+} nanospheres with Lu_2O_3(:Yb^{3+}) Shells

In brief, a certain amount of precursor Lu_2O_3:Yb^{3+}/Er^{3+} nanospheres were ultrasonically dispersed in water suspension, which contained $Lu(NO_3)_3$ ($Lu(NO_3)_3$/$Yb(NO_3)_3$) and $(NH_2)_2CO$ as a precipitant. The above suspensions were heated to 85°C and stirred for several hours to decompose the urea. Then, the resulting precursors were separated by centrifugation, washed several times with deionized water and ethanol, and dried at 80°C. Subsequently, the as-prepared amorphous core-shell samples were annealed at 850°C for 2 h in air to obtain the core-shell structured Lu_2O_3:Yb^{3+}/Er^{3+}@ Lu_2O_3(:Yb^{3+}) products.

Characterizations

The crystal structures and phase purities were analyzed by a Rigaku RU-200b X-ray powder diffractometer (XRD) using a nickel-filtered Cu-Ka radiation (λ = 1.5406 Å). The sizes and morphologies of the samples were investigated by Field emission scanning electron microscopy (FE-SEM, JEOL JSM-7500F) and transmission electron microscopy (TEM, Hitachi H-600). TGA curves were recorded by using a thermal analysis instrument (Perkine Elmer Pyris 1) with a heating rate of 10°C/min in a nitrogen flow of 100 mL/min. A Fourier transform infrared (FTIR) spectrometer (JASCOFT/IR-420) was used to record infrared spectra of the samples by using the KBr pellet technique. UCL spectra were recorded using a Hitachi F-4500 fluorescence spectrophotometer which equipped with a power-controllable 980 nm CW diode laser and detected by R928 photodetector (Hamamatsu). The temporal properties were studied by using a 953.6 nm Raman shifter laser and an oscillograph. All spectral measurements were performed at room temperature.

Results and discussion

The TEM images of the precursor samples are presented in Fig. 1. It is clear that the completely different morphologies can be obtained by using different precipitants. Fig. 1(a) shows that strongly agglomerated nanoparticles were formed by using NH_4OH as precipitant. In contrast, as shown in Fig. 1(b), while NH_4HCO_3 was selected as precipitant, the corresponding morphologies of the product were sub-micrometer wires. Furthermore, different form the above two cases, non-agglomerated spherical particles with nearly uniform size were formed in case of urea-based precipitation, as depicted in Fig. 1(c). The reason for these morphological changes can be attributed to the different hydrolysis rate of precipitants. Fig. 1(d) shows the corresponding XRD patterns of these precursor samples. It is obvious that amorphous precursors were formed by using NH_4OH and $(NH_2)_2CO$ as precipitants. Additionally, although several weak diffraction peaks appeared in case of NH_4HCO_3-based precipitation, two broad bands are still represented in XRD pattern Fig. 1(d2), which is corresponded to the amorphous structure as well.

Subsequent annealing is necessary to obtain crystalline samples and to investigate their luminescence properties. To select the appropriate annealing temperature in the experiments, the TGA curves of the precursor samples are measured, as shown in Fig. S1 (see ESI). From these curves, we observed obvious weight loss up to 850°C with the total weight loss are about 19.5%, 28.8%, and 26.7% for precursor samples prepared by NH_4OH, NH_4HCO_3, and $(NH_2)_2CO$ precipitants, respectively. On the basis of these TGA data, 850°C was selected as annealing temperature in the next work for obtaining crystalline phase of Lu_2O_3:Yb^{3+}/Er^{3+} samples.

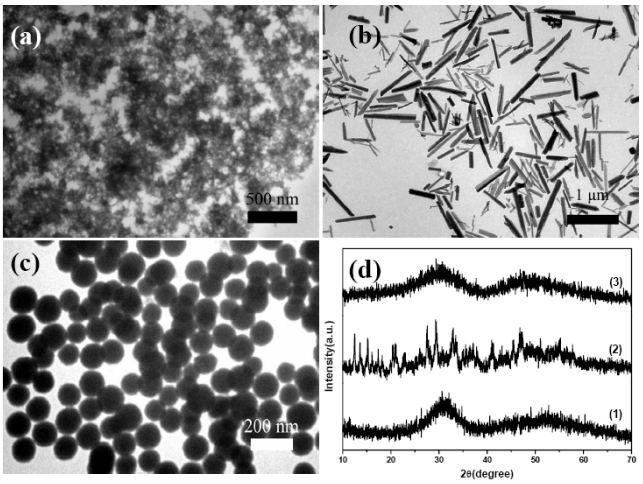

Fig. 1 TEM images of the precursor samples synthesis with (a) NH_4OH, (b) NH_4HCO_3, and (c) $(NH_2)_2CO$ precipitants; (d) XRD patterns of the precursor samples prepared with different precipitants (1) NH_4OH, (2) NH_4HCO_3, and (3) $(NH_2)_2CO$.

To illustrate the morphology change and the corresponding crystalline phases of the samples after heat treatment, the TEM images and XRD patterns were measured, as described in Fig. 2. For the samples annealed at 850°C, all the diffraction peaks can be well indexed to cubic phase Lu_2O_3 (JCPDS No.86-2475), as described in Fig. 2(d). No other impurity peaks can be detected from these three XRD patterns, indicating that the annealed samples are single-phased and RE^{3+} ions have effectively incorporated into the Lu_2O_3 host lattices. Additionally, compared with the corresponding precursor samples (Fig. 1(a–c)), the morphologies of Lu_2O_3 nano-aggregates, Lu_2O_3 sub-micrometer wires, and uniform Lu_2O_3 nanospheres are still sustained after anneal treatment, as shown in Fig. 2(a–c). It is worthwhile to point out that Lu_2O_3:Yb^{3+}/Er^{3+} nanocrystals synthesized in case of urea-based precipitation are nearly spherical in shape with uniform size (Fig. 3(c)), which is an appropriate object for investigating size dependence of UCL properties. Therefore, $(NH_2)_2CO$ was chosen as precipitant in the next work and different sizes of Lu_2O_3:Yb^{3+}/Er^{3+} nanospheres were prepared in the following sections for further investigations.

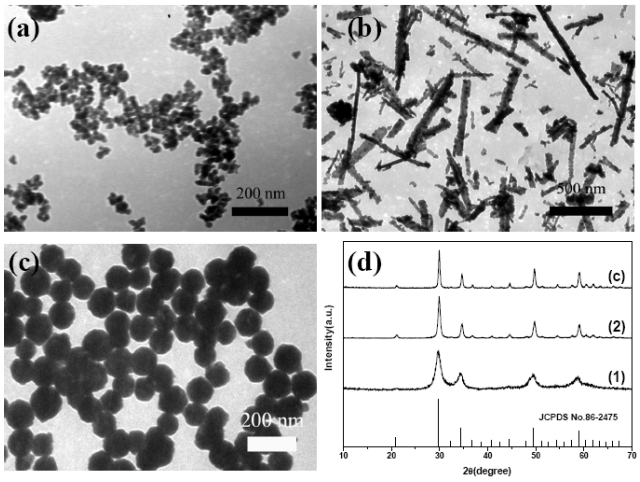

Fig. 2 TEM images of the annealed samples synthesis with (a) NH_4OH, (b) NH_4HCO_3, and (c) $(NH_2)_2CO$ precipitants; (d) XRD patterns of the annealed samples prepared with different precipitants (1) NH_4OH, (2) NH_4HCO_3, and (3) $(NH_2)_2CO$. The standard data for cubic Lu_2O_3 (JCPDS No.86-2475) is also presented in the figure for comparison.

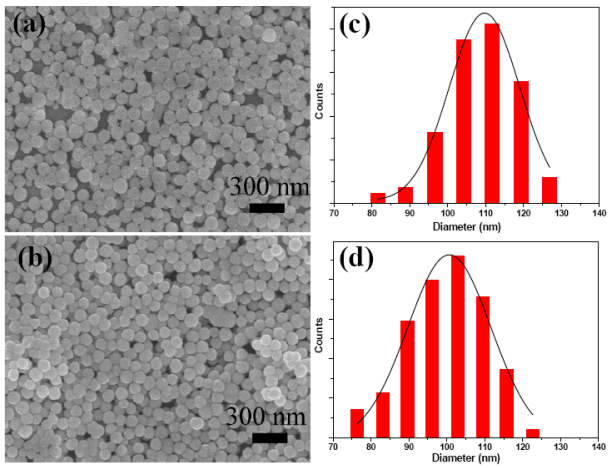

Fig. 3 SEM images of the (a) precursor and (b) annealed samples synthesis with $(NH_2)_2CO$ precipitant. The corresponding histograms of size distribution for the (c) precursor and (d) annealed Lu_2O_3:Yb^{3+}/Er^{3+} samples.

To further confirm the uniform size distribution of Lu_2O_3:Yb^{3+}/Er^{3+} nanospheres, SEM observations were performed. Fig. 3 (a) and (b) show the SEM micrographs of the samples without and with heat treatment, respectively. From the SEM micrographs, it is clear that the as-formed precursor sample consists of spherical particles with narrow size distribution (Fig. 3 (a)). After annealing treatment, we found that the crystallized Lu_2O_3 nanospheres are still spherical in shape and nearly uniform in size. However, the average size of these particles becomes slightly smaller than the precursor spheres, and the surfaces of these particles are not as smooth as the precursor ones. In addition, the corresponding histograms of size distribution for the precursor and annealed Lu_2O_3:Yb^{3+}/Er^{3+}, as depicted in Fig. 3 (c) and (d), respectively, further demonstrate the narrow size distributions of these two samples. Besides, after heat treatment, the obviously size reduction from 110 nm to 100 nm can be observed from these histograms as well.

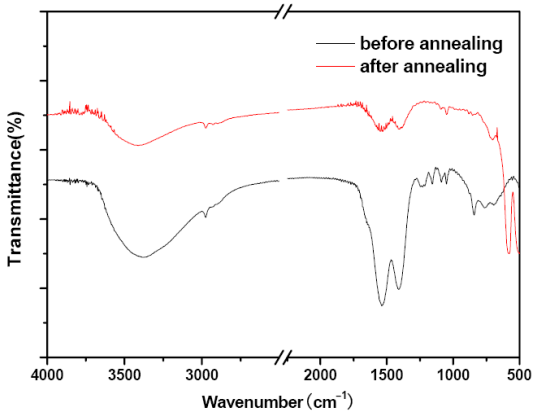

Fig. 4 FTIR spectra of the precursor (before annealing) and annealed (after annealing) samples prepared by using $(NH_2)_2CO$ precipitant.

The functional groups related with the surface information of the samples were examined by FTIR. The FTIR spectra for the precursor and annealed samples (by using urea as precipitant) are shown in Fig. 4. It is clear that both of them have the absorption band near 3378 cm^{-1}, which was assigned to stretching vibration of O–H band. Additionally, two intense bands at about 1537 cm^{-1} and 1410 cm^{-1} in both spectra are concerned with the asymmetric stretch of C–O in CO_3^{2-} groups. Furthermore, compared with the FTIR spectrum of the precursor sample, the new band at about 578 cm^{-1} in annealed sample can be assigned to the Lu–O stretching absorption of Lu_2O_3, which provides a powerful evidence for the formation of crystalline Lu_2O_3 nanocrystals after anneal treatment.

Table 1 The molar ratios of $[RE^{3+}]/(NH_2)_2CO$ for synthesizing Lu_2O_3:Yb^{3+}/Er^{3+} samples with different sizes.

Particle size	$[Ln^{3+}]$:urea (molar ratio)
250 nm	2.5×10^{-2}
200 nm	1.25×10^{-2}
165 nm	9×10^{-3}
100 nm	3×10^{-3}
45 nm	7.5×10^{-4}

To investigate the size dependence of UCL property, Lu_2O_3 nanospheres with different sizes and appropriate intervals were prepared by regulating the molar ratios of $[RE^{3+}]$ to $(NH_2)_2CO$. Table 1 shows the additive molar ratios of $[RE^{3+}]/(NH_2)_2CO$ for synthesizing Lu_2O_3:Yb^{3+}/Er^{3+} nanocrystals with different sizes. From the corresponding XRD patterns, as described in Fig. S2 (see ESI), we found that all the diffraction peaks of the samples are well indexed to cubic phase Lu_2O_3 (JCPDS No.86-2475). Fig. 5 presents the SEM micrographs of the (a–e) precursor and (f–j) annealed Lu_2O_3:Yb^{3+}/Er^{3+} samples synthesis with different ratios of $RE^{3+}/(NH_2)_2CO$. It is obvious that with decreasing the molar ratio of $[RE^{3+}]/(NH_2)_2CO$, the resultant Lu_2O_3 nanospheres become smaller and smaller. By decreasing the molar ratio of $[RE^{3+}]/(NH_2)_2CO$ to 7.5×10^{-4}, we observed that the width of diffraction peaks in XRD pattern become broad, as shown in Fig. S2(e), which further demonstrated the size reduction of Lu_2O_3 nanospheres. Additionally, as can be seen from Fig. 5(f–j), the nearly uniform-sized Lu_2O_3:Yb^{3+}/Er^{3+} nanospheres with the sizes of 250 nm, 200 nm, 165 nm, 100 nm, and 45 nm were obtained in the experiments.

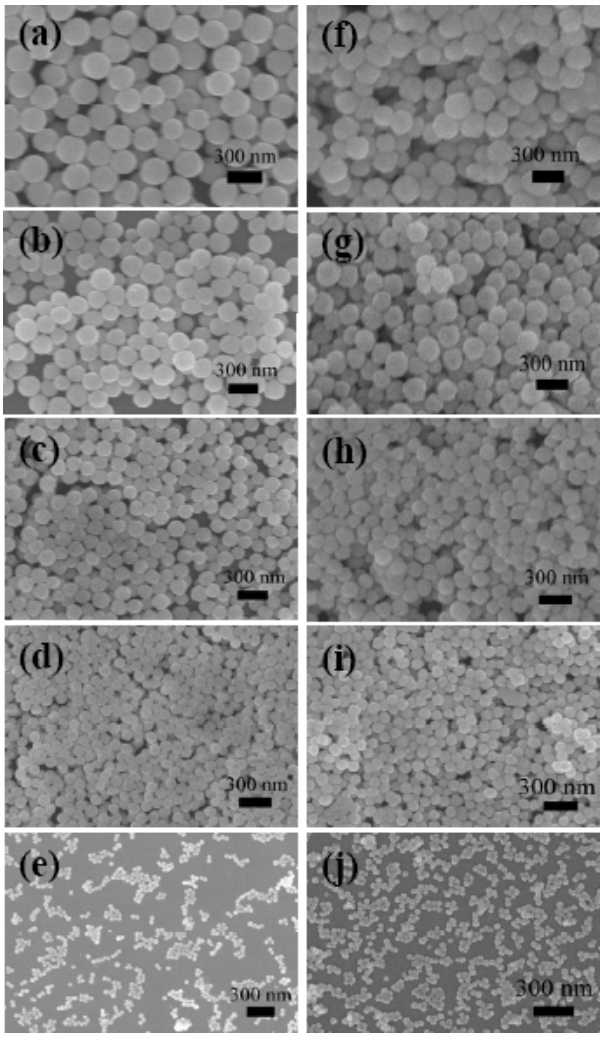

Fig. 5 SEM images of the (a–e) precursor and (f–j) annealed Lu_2O_3:Yb^{3+}/Er^{3+} samples synthesis with different ratios of $[RE^{3+}]/(NH_2)_2CO$. $[RE^{3+}]$:urea = 2.5×10^{-2} (a, f); 1.25×10^{-2} (b, g); 9×10^{-3} (c, h); 3×10^{-3} (d, i); 7.5×10^{-4} (e, j).

Figure 6 shows the FTIR spectra of the annealed Lu_2O_3:Yb^{3+}/Er^{3+} samples with different sizes. Obviously, the stretching adsorption of Lu–O (578 cm^{-1}), stretching vibration of O–H (3378 cm^{-1}), and asymmetric stretch of C–O (1537 cm^{-1}/1410 cm^{-1}) can be observed in all samples. Additionally, it is worthwhile to note that the intensities of these absorption bands increased with decreasing the particle size. This result can be well explained by surface effect as following: the specific area of a Lu_2O_3 nanosphere increased gradually with decreasing the particle size of Lu_2O_3 sample. Therefore, with the decrease of the particle sizes, the attached groups, such as CO_3^{2-} and OH^-, increased in the Lu_2O_3:Yb^{3+}/Er^{3+} samples and resulted in the increase of absorption intensities of the O–H and C–O bands.

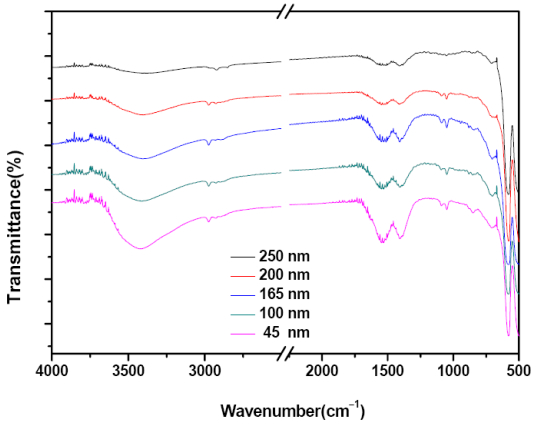

Fig. 6 FTIR spectra of the annealed Lu_2O_3:Yb^{3+}/Er^{3+} samples with different sizes.

Figure 7 displays the UCL spectra of Lu_2O_3:Yb^{3+}/Er^{3+} nanospheres with different sizes. Under 980 nm excitation, the sharp peaks in the green (515 – 580 nm) and red (635 – 700 nm) regions, which assign to the $^2H_{11/2}/^4S_{3/2} \rightarrow {}^4I_{15/2}$ and $^4F_{9/2} \rightarrow {}^4I_{15/2}$ transitions of Er^{3+} ions, respectively, are depicted in Fig. 7 clearly.[40, 41] It is obvious that both the green and red luminescence intensities decreased drastically with decreasing the size of Lu_2O_3:Yb^{3+}/Er^{3+} nanospheres. Compared with the luminescence intensities of Lu_2O_3:Yb^{3+}/Er^{3+} nanospheres with size of 250 nm, the green and red UCL decrease ~20 times and ~6 times, respectively, by intensities in 45 nm Lu_2O_3 nanospheres.

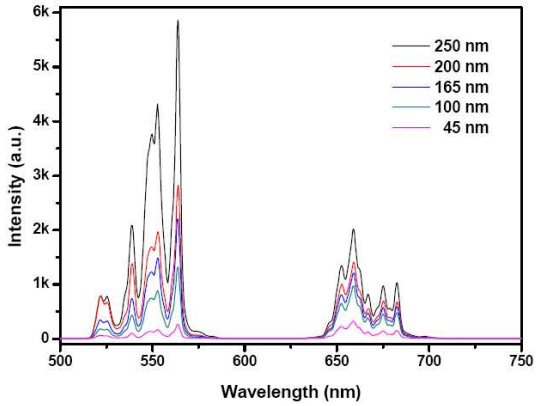

Fig. 7 UCL spectra of Lu_2O_3:Yb^{3+}/Er^{3+} nanocrystals with different particle sizes.

To further discuss the size dependence of UCL of Er^{3+}, the intensities of red emissions are normalized in UCL spectra, as depicted in Fig. 8(a). From Fig. 8(a), we can conclude that the relative intensity of green emission decreased gradually with the decrease of Lu_2O_3 particle size. Fig. 8(b) gives the intensity proportions of I_{green}/I_{red}, where I_{green} and I_{red} represent the green emission intensity and red emission intensity, respectively. It is clear that the I_{green}/I_{red} decreased gradually with the reduction of particle size. The above results can be mainly attributed to the surface effect and the specific explanations will be given in the following sections. Besides, to measure the color of the visible emissions, the chromaticity coordinates were calculated from the spectra by the method using the 1931 CIE system. As shown in the inset of Fig. 8(b), with the average particle size changed from 250 nm to 45 nm, the UCL can be controlled to some extent and the chromaticity coordinates (x, y) changed systematically from (0.343, 0.646) to (0.396, 0.593), corresponding to color points of the samples changed gradually from green to yellowish green.

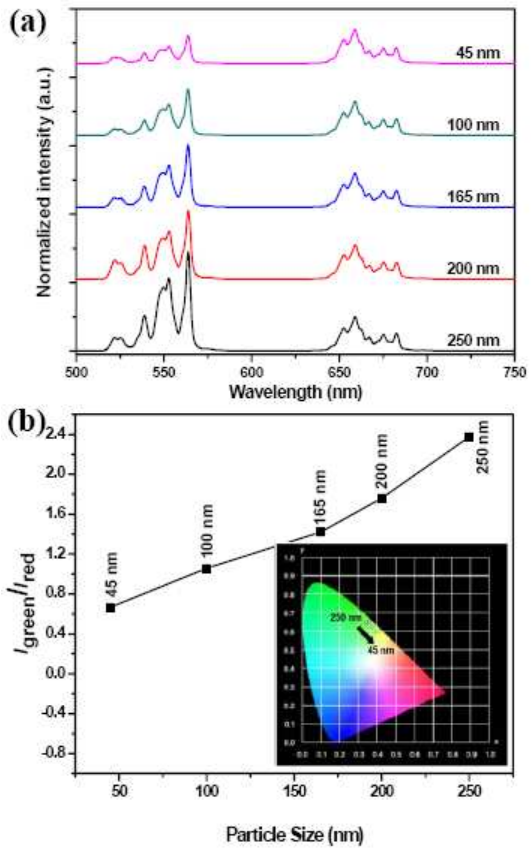

Fig. 8 (a) Normalized UCL spectra of Lu_2O_3:Yb^{3+}/Er^{3+} nanocrystals with different sizes. (b) The relationship between I_{green}/I_{red} and the sizes of Lu_2O_3:Yb^{3+}/Er^{3+} nanocrystals. Inset is the corresponding calculated color coordinates with decreasing the size of Lu_2O_3:Yb^{3+}/Er^{3+} nanocrystals from 250 to 45 nm.

To shed light on the UC mechanism well, we investigated the pump power I_{IR} dependence of UCL intensity I_f. For an unsaturated UC process, $I_f \propto I_{IR}^n$, where n is the number of IR photons absorbed per upconverted photon emitted.[42] Fig. S3 (see ESI) depicts the double logarithmic plots of I_f as a function of I_{IR} where the n values can be easily obtained from linear fit. For the

green emissions, the values of *n*s were calculated to be 1.85, 2.00, 2.16, 2.62, and 2.72 for the samples with sizes of 250, 200, 165, 100, and 45 nm, respectively. For the red emission, the corresponding *n*s were determined to be 1.67, 1.72, 1.95, 2.24, and 2.42. It is interesting to observe that the obtained *n*s for both green and red emissions increased with the reduction of particle sizes, and the *n*s obtained for the red emissions are smaller than those for the green emissions in all the samples.

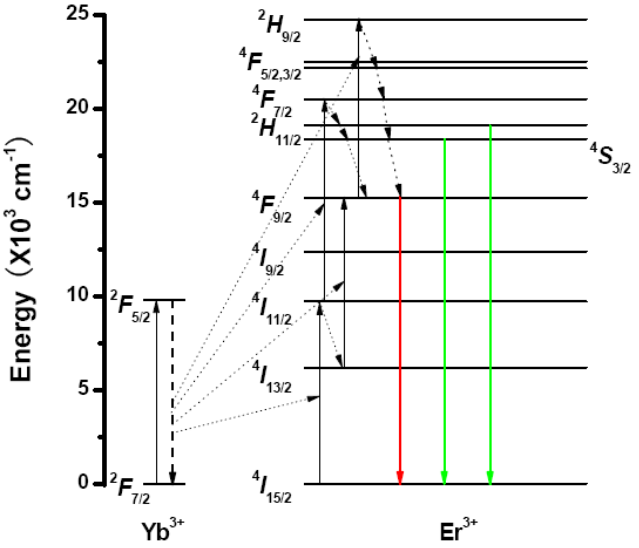

Fig. 9 Energy level diagrams of Yb^{3+} and Er^{3+} ions, and possible UC processes.

In Yb^{3+}-Er^{3+} codoped Lu_2O_3 samples and under 980 nm excitation, there are many different processes to populate the excited states of Er^{3+} ions.[43] Figure 9 shows the energy level diagrams of Yb^{3+} and Er^{3+} ions as well as the possible UC processes. Compared with Er^{3+}, Yb^{3+} has a higher doping concentration and a much larger absorption cross section around 980 nm, therefore, the main pathway to populate the excited states of Er^{3+} is the energy transfer (ET) from Yb^{3+} to Er^{3+}. Two characteristic routes have been proposed for populating the excited green and red levels of Er^{3+} in Yb^{3+}-Er^{3+} codoped systems, which described as follows: route 1: $^4I_{15/2} \rightarrow {}^4I_{11/2} \rightarrow {}^4F_{7/2} \rightarrow {}^2H_{11/2}$, $^4S_{3/2} \rightarrow {}^4F_{9/2}$; route 2: $^4I_{15/2} \rightarrow {}^4I_{11/2} \rightarrow {}^4I_{13/2} \rightarrow {}^4F_{9/2} \rightarrow {}^2H_{9/2} \rightarrow {}^2H_{11/2}$, $^4S_{3/2} \rightarrow {}^4F_{9/2}$.[14, 15] Obviously, a series of nonradiative relaxation (NR) processes, such as $^4I_{11/2} \rightarrow {}^4I_{13/2}$ and $^2H_{11/2}$, $^4S_{3/2} \rightarrow {}^4F_{9/2}$, *etc*, are involved and played important roles in populating the green and red levels of Er^{3+}. For the NR process of $^4I_{11/2} \rightarrow {}^4I_{13/2}$, it is well known that the energy gap (ΔE) between the upper and lower states (~3500 cm^{-1}) can be compensated by the energy came from the surface group OH^- efficiently.[15, 44] As discussed above (Fig. 6), the smaller particle size, the more surface functional groups. Therefore, with the decrease of particle sizes, the amounts of surface groups gradually increased and the NR process of $^4I_{11/2} \rightarrow {}^4I_{13/2}$ became more and more effective in the Lu_2O_3:Yb^{3+}/Er^{3+} nanocrystals. Based on this perspective, several experimental results, as described above, can be fully explained. Firstly, the NR process of $^4I_{11/2} \rightarrow {}^4I_{13/2}$ can resulted in the population at $^4I_{13/2}$ level increased while the population in the $^4I_{11/2}$ decreased. With another ET process of $^4I_{13/2} \rightarrow {}^4F_{9/2}$, enhanced red emission can be obtained in small particles. In contrary, with the ET of $^4I_{11/2} \rightarrow {}^4F_{7/2}$ and the following NR of $^4F_{7/2} \rightarrow {}^2H_{11/2}$, $^4S_{3/2}$, the related green emission intensity decreased with the reduction of particle size. Therefore, the luminescence ratio of I_{green}/I_{red} decreased gradually with the decrease of particle size, as shown in Fig. 8. Secondly, with decreasing the size of Lu_2O_3 particle to some extent, the route 2 described above is dominant in populating the green levels of Er^{3+} due to the efficient NR of $^4I_{11/2} \rightarrow {}^4I_{13/2}$. Thirdly, as deduced from route 2, three 980 nm photons are needed to populate the green levels, thus, the corresponding *n*s, as shown in Fig. S3 (see ESI), are larger than 2 in small particles.

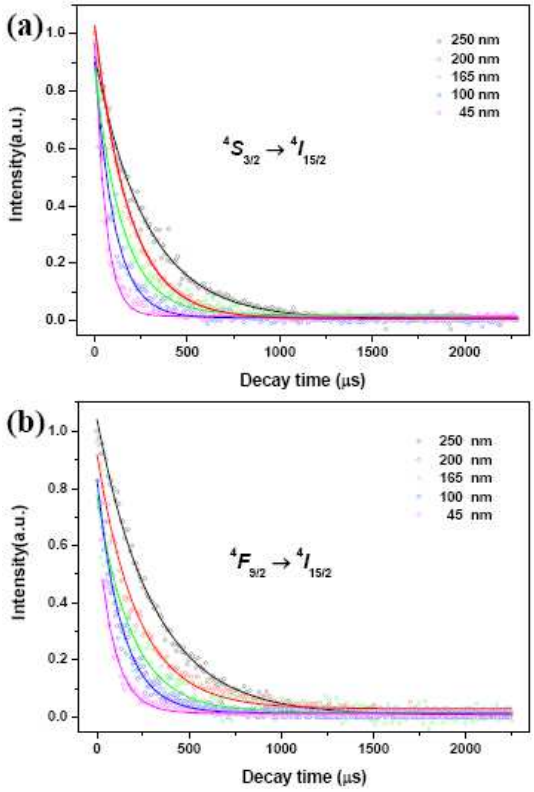

Fig. 10 Luminescence decay curves of Er^{3+} in Lu_2O_3:Yb^{3+}/Er^{3+} nanocrystals with different sizes. Open circles: experimental data; solid lines: fitting results by $I_{(t)} = I_0\exp(-t/\tau)$. (a) $^4S_{3/2} \rightarrow {}^4I_{15/2}$ transition; (b) $^4F_{9/2} \rightarrow {}^4I_{15/2}$ transition.

Table 2 The molar ratios of $[RE^{3+}]/(NH_2)_2CO$ for synthesizing Lu_2O_3:Yb^{3+}/Er^{3+} samples with different sizes.

Particle size	$^4S_{3/2}$/μs	$^4F_{9/2}$/μs
250 nm	278	308
200 nm	185	221
165 nm	147	186
100 nm	106	136
45 nm	57	92

To further confirm the surface effect and the size-dependent UCLs in Lu_2O_3:Yb^{3+}/Er^{3+} nanospheres, dynamic decay data are measured and analyzed. Fig. 10(a) and (b) show the luminescence decay curves of $^4S_{3/2} \rightarrow {}^4I_{15/2}$ and $^4F_{9/2} \rightarrow {}^4I_{15/2}$ transitions of Er^{3+}

ions in Lu_2O_3:Yb^{3+}/Er^{3+} nanospheres with different sizes, respectively. Each of the decay curves in Fig. 10 can be fitted well by single exponential function $I_{(t)} = I_0\exp(-t/\tau)$, where τ is the lifetime. The lifetime τs for the $^4S_{3/2}$ and $^4F_{9/2}$ states of Er^{3+} are described in Table 2. Obviously, with decreasing the sizes of Lu_2O_3 samples, the lifetime τs for the green and red levels of Er^{3+} shorten gradually. In addition, the values of τs obtained for green emission are shortened with respect to those obtained for red emission in all samples. Since all of the differently-sized Lu_2O_3:Yb^{3+}/Er^{3+} samples were prepared with the same concentration ratio (5mol%Yb^{3+} and 1mol%Er^{3+}) and with the same experimental conditions, the difference due to the dopants ratios and the experimental parameters on the dynamic measurements can be neglected. As we all know, the intrinsic radiative decay rates of Er^{3+} are almost the same for Lu_2O_3:Yb^{3+}/Er^{3+} samples with different sizes and the rates of nonradiative decay play crucial roles in affecting the total decay lifetime τ. Generally, the more surface functional groups are (the smaller particle size is), the faster nonradiative decay rate is. Therefore, with the reduction of particle size, the total decay times from $^4S_{3/2}$ and $^4F_{9/2}$ states of Er^{3+} ions gradually decreased, as depicted in Fig. 10 and Table 2, and the dynamic decay results provide another powerful evidence for the surface effect in Lu_2O_3 samples as well.

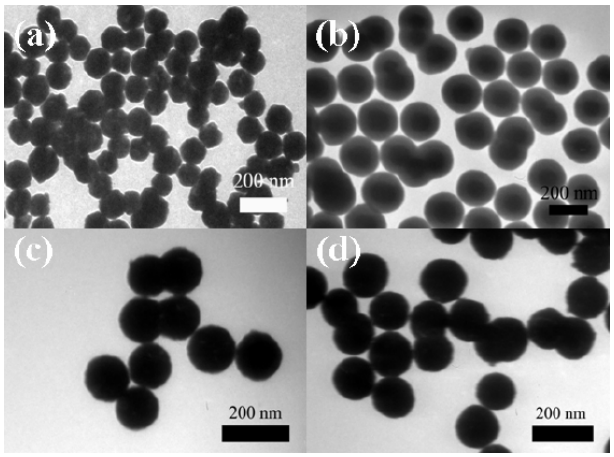

Fig. 11 TEM images of Lu_2O_3:Yb^{3+}/Er^{3+} nanocrystals with different surface coating. (a) pure Lu_2O_3:Yb^{3+}/Er^{3+} nanocrystals; (b) coating with SiO_2 shell; (c) coating with Lu_2O_3 shell; (d) coating with Lu_2O_3:Yb^{3+} shell.

Surface coating is an effective way to change the surface characteristic of the sample. At this end, we would like to discuss the UCL properties of Er^{3+} in Lu_2O_3:Yb^{3+}/Er^{3+} nanospheres with different shell coating. As a representative example, Lu_2O_3:Yb^{3+}/Er^{3+} nanospheres with the average size of 100 nm are selected here as cores, and the shell materials are silica, lutetium oxide, and Yb^{3+} doped lutetium oxide, respectively. Fig. 11 shows the TEM images of pure Lu_2O_3:Yb^{3+}/Er^{3+} nanocrystals (a) and the related core-shell samples of Lu_2O_3:Yb^{3+}/Er^{3+}@SiO_2 (b), Lu_2O_3:Yb^{3+}/Er^{3+}@Lu_2O_3 (c), and Lu_2O_3:Yb^{3+}/Er^{3+}@Lu_2O_3:Yb^{3+} (d). After coating with surface shells, it is obvious that the obtained samples are still spherical in shape and uniform in size, and the average sizes of these core-shell particles (Fig. 11(b–d)) become larger than the pure Lu_2O_3:Yb^{3+}/Er^{3+} spheres (Fig. 11(a)).

In addition, the corresponding XRD patterns of these core-shell samples are depicted in Fig. S4 (see ESI). From these XRD patterns, we observed that all the diffraction peaks can well be indexed to cubic phase Lu_2O_3. Moreover, a weak and broad band centered at 22°, as shown in Fig. S4(b), is the characteristic peak for amorphous SiO_2.

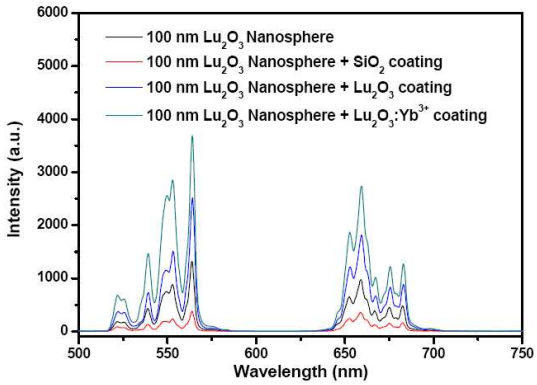

Fig. 12 UCL spectra of Lu_2O_3:Yb^{3+}/Er^{3+} nanocrystals with coating different surface shells.

Figure 12 shows the UCL spectra of pure Lu_2O_3:Yb^{3+}/Er^{3+} nanocrystals and the related core-shell samples. Compared with pure Lu_2O_3:Yb^{3+}/Er^{3+} nanospheres, the emission intensity of the sample coated with SiO_2 was greatly decreased, while the UCL intensities of Lu_2O_3:Yb^{3+}/Er^{3+}@Lu_2O_3(:Yb^{3+}) nanocrystals were increased, as described in Fig. 12. On one hand, the decrease of emission intensity by SiO_2 coating can well be explained by lattice mismatch between Lu_2O_3 and SiO_2.[45, 46] On the other hand, for the enhanced UCLs in Lu_2O_3(:Yb^{3+}) coating samples, some of possible reasons can be proposed as follows: as discussed above, the larger particle size is, the lower nonradiative decay possibility is. Fig. 11(c) and (d) confirmed that the particle sizes of core-shell samples are lager than that of pure Lu_2O_3:Yb^{3+}/Er^{3+} nanocrystals. Therefore, the NR processes decreased in core-shell samples, resulting the UCL intensities greatly increased in Lu_2O_3:Yb^{3+}/Er^{3+}@Lu_2O_3(:Yb^{3+}) samples. Furthermore, it is interesting to observe in Fig. 12 that the additional adding of Yb^{3+} in shell layer is beneficial for the enhancement of UCL of Er^{3+}. As deduced from Fig. 11(c) and (d), the samples coating with Lu_2O_3 and Lu_2O_3:Yb^{3+} are nearly the same in their sizes, therefore, the difference of UCL intensities due to the particle size should not be considered here. The enhanced UCL by coating with Lu_2O_3:Yb^{3+} shells can be attributed to the effective increment of quenching concentration of Yb^{3+} in such core-shell structure, which facilitates the ETs between sensitizer (Yb^{3+}) and activator (Er^{3+}), and the similar explanation has been addressed well in other previous works.[47–49]

Table 3 The molar ratios of $[RE^{3+}]/(NH_2)_2CO$ for synthesizing Lu_2O_3:Yb^{3+}/Er^{3+} samples with different sizes.

Sample	$^4S_{3/2}$/μs	$^4F_{9/2}$/μs
100 nm Lu_2O_3 Nanosphere	106	136
SiO_2 coating	82	96
Lu_2O_3 coating	159	192
Lu_2O_3:Yb^{3+} coating	223	272

Finally, we investigated the dynamic decay behaviors of these core-shell samples. The luminescence decay curves of Er^{3+} in Lu_2O_3:Yb^{3+}/Er^{3+} nanospheres coating with different surface shells are shown in Fig. S5 (see ESI). All of the decay curves can be fitted well by $I_{(t)} = I_0\exp(-t/\tau)$ and the corresponding lifetime τs are shown in Table 3. Generally, for the active ions in UCL materials, a short lifetime usually means the low luminescence efficiency.[50] Thus, as depicted in Fig. S4 and Table 3, the lifetime τs for the green and red levels of Er^{3+} shorten gradually with the decrease of UCL intensity.

Conclusions

In conclusion, a simple and effective homogeneous precipitation method followed by annealing at high temperature has been developed to synthesize Lu_2O_3:Yb^{3+}/Er^{3+} nanocrystals. Spherical Lu_2O_3:Yb^{3+}/Er^{3+} nanoparticles with nearly uniform size were obtained by using urea as precipitant. By regulating the molar ratios of $[RE^{3+}]/(NH_2)_2CO$, Lu_2O_3:Yb^{3+}/Er^{3+} nanospheres with the sizes of 45 nm, 100 nm, 165 nm, 200 nm, and 250 nm were successfully synthesized in the experiments. Under the excitation of 980 nm, green ($^2H_{11/2}$/$^4S_{3/2} \rightarrow {}^4I_{15/2}$) and red ($^4F_{9/2} \rightarrow {}^4I_{15/2}$) UCLs of Er^{3+} were observed in these Lu_2O_3:Yb^{3+}/Er^{3+} nanospheres. With decreasing the particle sizes of Lu_2O_3 nanospheres, both of the total UCL intensities and the intensity ratios of I_{green}/I_{red} decreased gradually. The absorption intensities of O–H and C–O bands increased with decreasing the size of Lu_2O_3 nanocrystals, resulting in the efficient NR process of $^4I_{11/2} \rightarrow {}^4I_{13/2}$ in small particles. Surface effect and the possibility of NR process of $^4I_{11/2} \rightarrow {}^4I_{13/2}$ were proposed to explain the size-dependent UCL properties. The decay times for the $^4S_{3/2}$ and $^4F_{9/2}$ states of Er^{3+} shorten gradually with decreasing the size of Lu_2O_3:Yb^{3+}/Er^{3+} nanospheres. By coating Lu_2O_3:Yb^{3+}/Er^{3+} nanospheres with SiO_2 shells, UCL of Er^{3+} was decreased drastically owing to the lattice mismatch between Lu_2O_3 and SiO_2. In contrast, instead of coating with Lu_2O_3(:Yb^{3+}) shells, the UCL intensities of Er^{3+} was greatly increased, which can be attributed to the increase of particle sizes and the decrease of surface groups. Compared with the luminescence intensity of Er^{3+} in Lu_2O_3:Yb^{3+}/Er^{3+}@Lu_2O_3 nanocrystals, enhanced UCL of Er^{3+} was obtained by adding additional Yb^{3+} into shell layers. In these core-shell samples, the lifetime τs for the green and red levels of Er^{3+} shorten gradually with the decrease of UCL intensity as well.

Acknowledgments

The authors are thankful for the financial support of the National Natural Science Foundation of China (NNSFC) (grants 51072056, 61178073, 11274139, and 60908031), China Postdoctoral Science Foundation (2012M520668).

Notes and references

State Key Laboratory on Integrated Optoelectronics, College of Electronic Science and Engineering, Jilin University, Changchun 130012, China. Fax: +86-431-85168241-8325; Tel: +86-431-85153853; E-mail: wpqin@jlu.edu.cn.

1 F. Auzel, *Chem. Rev*. 2004, **104**, 139.
2 F. Wang, X. Liu, *Chem. Soc. Rev.* 2009, **38**, 976.
3 S. Heer, K. Kömpe, H. Güdel, and M. Haase, *Adv. Mater*. 2004, **16**, 2102.
4 K. Kramer, D. Biner, G. Frei, H. Güdel, M. Hehlen, and S. Luthi, *Chem. Mater.* 2004, **16**, 1244.
5 D. Chen, L. Lei, A. Yang, Z. Wang, and Y. Wang, *Chem. Commun*. 2012, **48**, 5898.
6 M. Haase, H. Schäfer, *Angew. Chem. Int. Ed*. 2011, **50**, 5808.
7 F. Wang, Y. Han, C. Lim, Y. Lu, J. Wang, J. Xu, H. Chen, C. Zhang, M. Hong, and X. Liu, *Nature* 2010, **463**, 1061.
8 T. Hebert, R. Wannemacher, W. Lenth, and R. Macfarlane, *Appl. Phys. Lett*. 1990, **57**, 1727.
9 P. Kannan, F. Rahim, R. Chen, X. Teng, L. Huang, H. Sun, and D. Kim, *ACS Appl. Mater. Interfaces*, 2013, **5(9)**, 3508.
10 Y. Liu, M. Chen, T. Cao, Y. Sun, C. Li, Q. Liu, T. Yang, L. Yao, W. Feng, and F. Li, *J. Am. Chem. Soc.* 2013**, 135**, 9869.
11 Y. Liu, D. Tu, H. Zhu, R. Li, W. Luo, and X. Chen, *Adv. Mater*. 2010, **22**, 3266.
12 L. Lei, D. Chen, P. Huang, J. Xu, R. Zhang, and Y. Wang, *Nanoscale*. 2013, **5**, 11298.
13 D. Chen, Y. Wang, *Nanoscale*. 2013, **5**, 4621.
14 K. Zheng, L. Wang, D. Zhang, D. Zhao, and W. Qin, *Opt. Express* 2010, **18**, 2934.
15 H. Song, B. Sun, T. Wang, S. Lu, L. Yang, B. Chen, X. Wang, and X. Kong, *Solid State Commun*. 2004, **132**, 409.
16 H. Guo, N. Dong, M. Yin, W. Zhang, L. Lou, and S. Xia, *J. Phys. Chem. B* 2004, **108**, 19205.
17 León-Luis, F. Sergio, Rodríguez-Mendoza, R. Ulises, Emmanuel. Lalla, Víctor. Lavín, *Sensors and Actuators B* 2011**, 158**, 208–213.
18 K. Zheng, Z. Liu, Y. Liu, W. Song, and W. Qin, *J. Appl. Phys.* 2013, **114**, 183109.
19 D. Chen, L. Lei, J. Xu, A. Yang, and Y. Wang, *Nanotechnology*. 2013, **24**, 085708.
20 E. Zych, D. Hreniak, and W. Strek, *J. Phys. Chem. B* 2002, **106**, 3805.
21 J. Lu, K. Takaichi, T. Uematsu, A. Shirakawa, M. Musha, K. Ueda, H. Yagi, T. Yanagitani, and A. Kaminskii, *Appl. Phys. Lett*. 2002, **81**, 4324.
22 J. Boyer, F. Vetrone, J. Capobianco, A. Speghini, and M. Bettinelli, *J. Phys. Chem. B* 2004, **108**, 20137.
23 E. Zych, J. Trojan-Piegza, D .Hreniak, and W. Strek, *J. Appl. Phys.* 2003, **94**, 1318.
24 G. Scarel, E. Bonera, C. Wiemer, G. Tallarida, S. Spiga, M. Fanciulli, I. Fedushkin, H. Schumann, Y. Lebedinskii, and A. Zenkevich, *Appl. Phys. Lett*. 2004, **85**, 630.
25 J. Yang, C. Zhang, C. Peng, C. Li, L. Wang, R. Chai, and J. Lin, *Chem - Eur. J*, **2009**, **15**, 4649.
26 Y. Li, J. Zhang, X. Zhang, Y. Luo, X. Ren, H. Zhao, X. Wang, L. Sun, and C. Yan, *J. Phys. Chem. C* 2009, **113**, 4413.
27 J. Yang, C. Li, Z. Quan, C. Zhang, P. Yang, Y. Li, C. Yu, and J. Lin, *J. Phys. Chem. C* 2008, **112**, 12777.
28 G. Jia, Y. Zheng, K. Liu, Y. Song, H. You, and H. Zhang, *J. Phys. Chem. C* 2009, **113**, 153.
29 O. Guillot-Noël, B. Bellamy, B. Viana, and D. Vivien, *Phys. Rev. B: Condens. Matter Mater. Phys.* 1999, **60**, 1668.
30 F. Vetrone, J. Boyer, J. Capobianco, A. Speghini, and M. Bettinelli, *J. Phys. Chem. B* 2002, **106**, 5622.
31 H. Zhang, J. Liu, J. Wang, X. Xu, and M. Jiang, *Appl. Opt.* 2005**, 44**, 7439.
32 B. Walsh, G. Grew, and N. Barnes, *J. Phys.: Condens. Matter.* 2005, **17**, 7643.
33 M. Sugiyama, T. Yanagida, Y. Yokota, S. Kurosawa, Y. Fujimoto, and A. Yoshikawa, *Radiat. Meas.* 2013, **55**, 112.
34 F. Jing, K. Shimamura, E. Villora, A. Medvedev, K. Kitamura, K. Asai, and A. Sato, *J. Am. Ceram. Soc.* 2008, **91**, 296.
35 N. Sarukura, Z. Liu, Y. Segawa, K. Edamatsu, Y. Suzuki, T. Itoh, V. Semashko, A. Naumov, S. Korableva, R. Abdulsabirov, and M. Dubinskii, *Opt. Lett.* 1995, **20**, 294.
36 F. Shi, J. Wang, X. Zhai, D. Zhao, and W. Qin, *CrystEngComm*. 2011**, 13**, 3782.
37 Q. Liu, Y. Sun, T. Yang, W. Feng, C. Li, and F. Li, *J. Am. Chem. Soc.* 2011**, 133**, 17122.
38 N. Dulina, Y. Yermolayeva, A. Tolmachev, Z. Sergienko, O. Vovk, E.

Vovk, N. Matveevskaya, and P. Mateychenko, *J. Eur. Ceram. Soc.* 2010**, 30**, 1717.
39 W. Stöber, A. Fink, and E. Bohn, *J. Colloid Interface Sci*. 1968, **26**, 62.
40 G. Yi,; G. Chow, *Adv. Mater*. 2006, **16**, 2324.
41 K. Zheng, D. Zhao, D. Zhang, N. Liu, and W. Qin, *Opt. Lett.* 2010, **35**, 2442.
42 M. Pollnau, D. Gamelin, S. Lüthi, H. Güdel, M. Hehlen, *Phys. Rev. B* 2000, **61**, 3337.
43 W. Carnall, P. Fields, K. Rajnak, *J. Chem. Phys.* 1968**, 49**, 4424.
44 X. Bai, H. Song, G. Pan, Y. Lei, T. Wang, X. Ren, S. Lu, B. Dong, Q. Dai, and L. Fan, *J. Phys. Chem. C* 2007, **111**, 13611.
45 J. Shan, Y. Ju, *Appl. Phys. Lett*. 2007, **91**, 123103.
46 L. Liang, Y. Liu, C. Bu, K. Guo, W. Sun, N. Huang, T. Peng, B. Sebo, M. Pan, W. Liu, S. Guo, and X. Zhao, *Adv. Mater*. 2013, **25**, 2174.
47 P. Ghosh, J. Oliva, E. De la Rosa, K. Haldar, D. Solis, and A. Patra, *J. Phys. Chem. C* 2008, **112**, 9650.
48 F. Vetrone, R. Naccache, V. Mahalingam, C. Morgan, J. Capobianco, *Adv. Funct. Mater*. 2009, **19**, 2924.
49 D. Yang, C. Li, G. Li, M. Shan, X. Kang, and J. Lin, *J. Mater. Chem*. 2011, **21**, 5923.
50 F. Shi, J. Wang, D. Zhang, G. Qin, and W. Qin, *J. Mater. Chem*. 2011, **21**, 13413.